Taylor & Francis
Taylor & Francis Group

Coastal Engineering Journal

ISSN: 2166-4250 (Print) 1793-6292 (Online) Journal homepage: www.tandfonline.com/journals/tcej20

Applicability of ocean wave measurements based on high-frequency radar systems in an estuary region

Tomoya Kataoka & Takashi Fujiki

To cite this article: Tomoya Kataoka & Takashi Fujiki (2024) Applicability of ocean wave measurements based on high-frequency radar systems in an estuary region, Coastal Engineering Journal, 66:1, 58-73, DOI: 10.1080/21664250.2023.2275469

To link to this article: https://doi.org/10.1080/21664250.2023.2275469

COASTAL ENGINEERING JOURNAL
2024, VOL. 66, NO. 1, 58–73
https://doi.org/10.1080/21664250.2023.2275469

RESEARCH ARTICLE

Applicability of ocean wave measurements based on high-frequency radar systems in an estuary region

Tomoya Kataoka[a,b,c] and Takashi Fujiki[c]

[a]Department of Civil & Environmental Engineering, Ehime University, Matsuyama, Japan; [b]Center for Marine Environmental Studies, Ehime University, Matsuyama, Japan; [c]Marine Information Group, Port and Airport Research Institute, Yokosuka, Japan

ABSTRACT
The applicability of high-frequency (HF) radar systems for wave measurement in an estuary was explored by extracting the significant wave height (H_{sr}) using a traditional Barrick equation from the Doppler spectra observed by three radar systems installed in Ise Bay, Japan. The minimum value of H_{sr} estimated around each grid point was relatively consistent with the wave height observed with a wave gauge/buoy, except for a deterioration of wave measurement accuracy caused by a decrease in seawater conductivity from the freshwater inflow after flooding. Furthermore, the relationship between the accuracy and the signal-to-noise ratios for the first- and second-order peaks (SNR_1 and SNR_2, respectively) highlighted the difficulty in determining the threshold values of SNRs in the bay. Thus, we suggest the use of H_{sr} as a criterion for quality control when applying a nonlinear inversion method for estimating ocean wave spectra based on the Bayesian possibility theorem (BIM). Our suggestion is to select the appropriate Doppler spectra and increase the acquisition rates of wave data with low relative error compared to BIMs using SNR_1 and SNR_2. These results can promote the applicability of the nonlinear inversion in estuary regions.

ARTICLE HISTORY
Received 20 April 2023
Accepted 22 October 2023
Published online 1 November 2023

KEYWORDS
High-frequency radar; significant wave height; signal-to-noise ratio; seawater conductivity; Ise Bay

1. Introduction

The 3–30 MHz high-frequency (HF) radar system is a powerful tool for continuous monitoring of ocean currents and waves within 200 km of the coast at high spatial (1–6 km) and temporal (hourly or higher) resolutions (Roarty et al. 2019). The radar system can provide the Doppler spectrum, which consists of first- and second-order scattered powers (Barrick 1971, 1972a, 1972b). These scattered powers are proportional to the scattered cross-section. According to Barrick's theoretical expression, the first-order cross-section is determined by the wave energy of a fundamental wave whose wavenumber is twice the wavenumber in the beam direction of the radio wave (i.e. Bragg scattering wave). Moreover, the second-order cross-section is expressed by a nonlinear integral function in which the wave energies of pairs of fundamental waves are included.

Hasselmann (1971) first suggested that the second-order Doppler sidebands around each first-order peak should be proportional to the wave frequency spectra, but a root-mean-square wave height (H_{rms}) estimated following this suggestion was not strictly true based on a comparison with buoy measurements for true wave height (Barrick 1977a). Thus, Barrick 1977a, 1977b) employed a weighting function for the second-order backscattered power, which was obtained from theoretical models of electromagnetic and hydrodynamic coupling factors, and derived an equation to extract H_{rms} based on the ratio of the weighted second-order to the first-order powers, hereinafter referred to as the "Barrick equation." By applying the Barrick equation, Ramos, Graber, and Haus (2009) demonstrated the capability of phased-array HF radar systems to sample the spatial distribution of wave energy in different storm scenarios and coastal configurations. Subsequently, many algorithms have been proposed to invert the two-dimensional ocean wave spectrum based on a theoretical second-order cross-section equation (Green and Wyatt 2006; Guiomar and Conley 2019; Hashimoto and Tokuda 1999; Hisaki 2015; Wyatt and Jim Green 2009). Green and Wyatt (2006) inverted theoretical first- and second-order cross-section equations proposed by Barrick and Weber (1977) and Weber and Barrick (1977) by several row-action methods. Hisaki (2015) developed an algorithm for inverting the wave spectrum by solving these theoretical equations using several constraints. In another approach, Hashimoto and Tokuda (1999) developed a technique for inverting the wave spectrum with the Bayesian theorem (BIM) by assuming that the wave spectrum is smooth in both wave frequency and direction planes. Kataoka and Nagamatsu (2016) modified the BIM to invert the wave spectrum in shallow water.

The availability of wave Information based on these algorithms is dependent on the significant backscattered power induced by ocean waves, but the power could be contaminated due to internal/external noise.

CONTACT Tomoya Kataoka kataoka.tomoya.ab@ehime-u.ac.jp; tkata@cee.ehime-u.ac.jp

Thus, previous studies often used the signal-to-noise ratio (SNR) as a criterion for wave measurement (e.g. Tian et al. 2020; Wyatt et al. 2005, 2006). The SNRs for first- and second-order scattering (hereinafter referred to as SNR_1 and SNR_2, respectively) have been adopted as criteria. However, several threshold values existed in previous studies. Wyatt et al. (2005) asserted that wave measurement requires an SNR_2 of at least 10 dB. Thus, Wyatt et al. (2006) used Doppler spectra with $SNR_2 >15$ dB. Additionally, Tian et al. (2020) suggested that the threshold value of SNR_1 could be 20 dB for ocean current measurements.

However, these wave measurement algorithms have been rarely applied to monitor estuary regions because HF radio waves strongly attenuate due to the desalination of seawater, that is, the decline in seawater conductivity determined by the sea surface temperature (SST) and sea surface salinity (SSS) (Gurgel, Essen, and Kingsley 1999). In addition, the attenuation depends on the radio frequency and distance from the radar station (Gurgel, Essen, and Kingsley 1999). This could hinder HF radar-derived wave measurements in estuary regions. Nevertheless, monitoring waves is essential to manage marine transport, mitigate storm-induced coastal disasters, and operate fisheries in estuary regions. In this case, HF radar systems can be potentially significant tools to provide wave data if their applicability is sufficiently validated.

In the present study, the applicability of HF radar-derived wave measurements in estuary regions is validated in Ise Bay, which is a major estuary in Japan. For this purpose, the significant wave heights are computed by applying the Barrick equation to the Doppler spectra observed by three radar systems installed on the bay's coast. The calculated wave heights are evaluated by comparison with wave heights measured by a depth-mounted gauge and buoy. The deterioration of the wave measurement accuracy in the bay and the determinative factors are discussed. Following our findings, several criteria used to decide which Doppler spectra to invert using BIM are considered. This study provides suggestions for inverting the wave spectrum and insights into the deterioration of wave measurement accuracy in an estuary.

2. Materials and methods

2.1. Study area and periods

Our study area was Ise Bay, in the center of Japan (Figure 1), with an average depth of 16.8 m. The eastern region of the bay is called Mikawa Bay, and the total basin area of Ise Bay and Mikawa Bay is 16,191 km^2. The bay mouth is connected to the Pacific Ocean in the southern region of the bay. Seawater exchange is low because the bay mouth width is 12 km; the residence time is approximately one year. Freshwater flows into the bay from four rivers (Kiso, Nagara, Ibi, and Shounai Rivers) on the northern coast and four rivers (Suzuka, Kushida, Kumodzu, and Miya Rivers) on the western coast. The Kiso River is the largest river flowing into the bay, with a basin area of 5,275 km^2. The basin areas of the Nagara, Ibi, and Shonai Rivers are 1,985 km^2, 1,840 km^2, and 1,010 km^2, respectively. The bay's northern part of the catchment area is 10,110 km^2, corresponding to 62% of the whole area (16,191 km^2). Moreover, the basin areas of four rivers (Suzuka, Kushida, Kumodzu, and Miya Rivers) in the western parts are 2,254 km^2 (323 km^2, 461 km^2, 550 km^2, and 920 km^2, respectively), which corresponds to 14% of the whole area.

In the present study, five periods for the significant growth of ocean waves due to the presence of typhoons in Japan were selected as targets (p1: 16–September 26 2016; p2: 18–October 28 2017; p3: 19–August 29 2018; p4: 31 August–September 10 2018; p5: 26 September–October 6 2018; see Table 1). To evaluate the influence of the freshwater inflow from the eight rivers on the HF radar-derived wave measurement, we collected data on hourly river discharges at nine river-discharge stations (stations D1 to D9 in Figure 1) that were not in the tidal reach in each river during the periods via the Water Information System operated by MLIT (http://www1.river.go.jp/). Note that station D5 was in the Utsube River, the major tributary of the Suzuka River. As station D6 was located upstream of the confluence point, the river discharge of the Suzuka River was evaluated by summing those measured at stations D5 and D6. The peaks of the total river discharge ranged between 7,501 and 20,661 m^3/s in the five periods (Table 1); thus, the river discharge from three major rivers (Kiso, Nagara, and Ibi Rivers) in the Kiso River basin was predominant in the freshwater inflow. The largest flooding event occurred in period p1 (Figure 2).

2.2. Sea state monitoring stations in Ise Bay

Three HF radar systems (Nagano Japan Radio Company (NJRC)) were installed by the Ministry of Land, Infrastructure, Transport and Tourism, Japan (MLIT) in November 2005. Their central frequency for the transmission signal was 24.515 MHz with a sweep bandwidth of 100 kHz along the coast of Ise Bay (Figure 1). Doppler spectra with a spatial resolution of 1.5 km and an azimuth of 7.5° were observed in the bay. The beam directions of radars N, T, and O ranged between 164° and 246.5°, between 47° and 167°, and between −26.6° and 93.4°, respectively, in the clockwise direction from the north, and the numbers of beams were 12, 17, and 17, respectively. The three HF radar systems were operated at 10 min intervals, on the hour (Radar N), 10 min later (Radar T), and 20 min later (Radar O) every hour to avoid unexpected radio interference between the HF radars, for

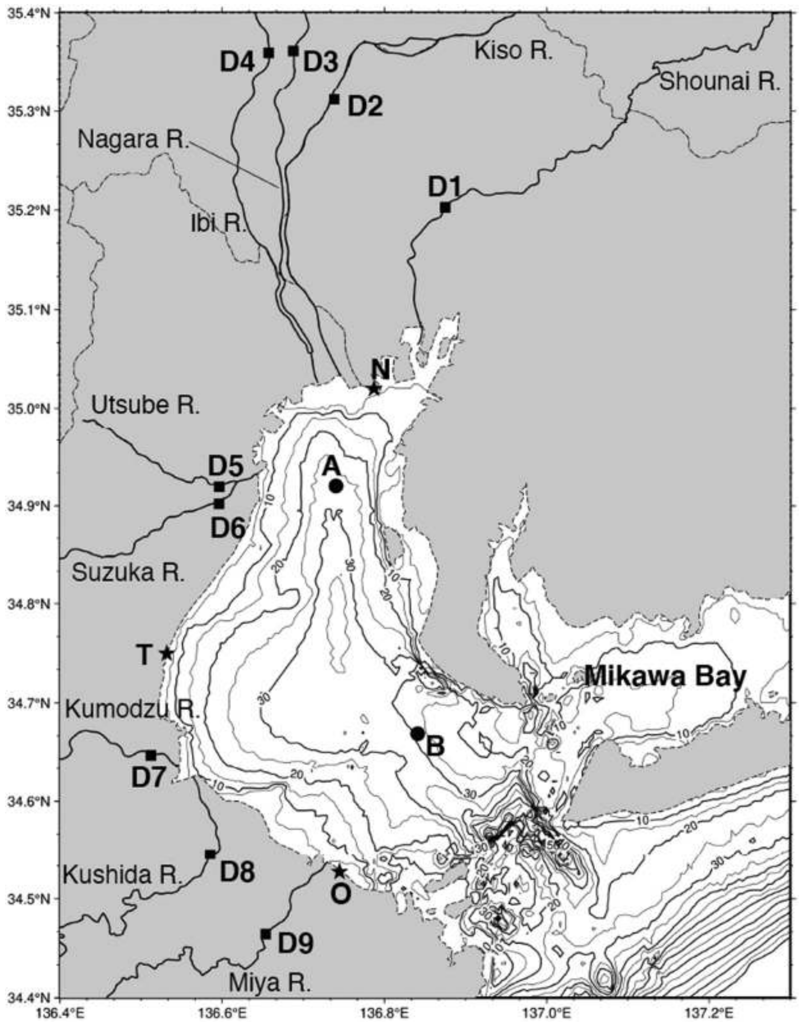

Figure 1. Study area. The stars are the three HF radar stations. The contour in the sea indicates the depth with 5 m intervals (thin line) and 10 m intervals (thick line). The squares are the monitoring sites of river discharge in nine major rivers flowing into the bay. The circles are locations where water quality parameters (seawater temperature and salinity) and wave heights are observed.

which the hourly Doppler spectra were available from the three HF radar systems.

Two monitoring stations were situated in the inner bay where surface waves provided in the Nationwide Ocean Wave information network for Ports and Harbours (NOWPHAS: https://www.mlit.go.jp/kowan/nowphas/index_eng.html) and water quality parameters (e.g. salinity and temperature) provided by MLIT were observed (black circles in Figure 1). Stn. A (Stn. B) was located at distances of 11.1 km (39.3 km) from radar N, 27.2 km (29.7 km) from radar T, and 44.5 km (18 km) from radar O. The depths at Stns. A and B were 27 m and 30 m, respectively. The seawater conductivity was calculated from SSS and SST observed at each station by the International Thermodynamic Equation of Seawater-2010 (IOC, SCOR, and IAPSO 2010) (Figure 2). Note that the pressure was negligible in the conversion of the seawater conductivity because the skin depth of radio waves at 25 MHz is on the order of a few centimeters (Halverson, Pawlowicz, and Chavanne 2017).

2.3. Extraction of significant wave height from Doppler spectra

First-order backscattering of the incident radio waves on the sea surface is induced by a Bragg scattering wave with $2k_0$ in the same direction, where k_0 is the radio wavenumber (Crombie 1955). In addition, second-order backscattering is induced by a bound wave that satisfies the following resonance condition:

$$\mathbf{k}_1 + \mathbf{k}_2 = -2\mathbf{k}_0 \tag{1}$$

where $\mathbf{k}_i (i = 1, 2)$ and $\mathbf{k}_0$ are the wavenumber vectors of the fundamental and radio waves, respectively. The first- and second-order cross-sections (σ_1 and σ_2) can be normalized by ω_b (i.e. $\sigma_{iN}(\omega_{DN}) = \omega_b \sigma_i(\omega_D)(i = 1, 2)$) as Eqs. (2) and (3), respectively (Hisaki 1996; Lipa and Barrick 1986).

$$\sigma_{1N}(\omega_{DN}) = 4\pi S_N(-m_2\mathbf{n})\delta(\omega_{DN} - m_2), \tag{2}$$

Table 1. Summary of river discharge peak, freshwater inflow volume from northern and western rivers and mean sea water conductivity at Stns. A and B in the five periods.

			Northern rivers			Western rivers			Stn. A			Stn. B		
No	Duration	Total peak discharge [m^3/s]	Date	Peak discharge [m^3/s]	Freshwater volume [×10^9 m^3]	Date	Peak discharge [m^3/s]	Freshwater volume [×10^9 m^3]	Conductivity (Before)*1	Conductivity (After)*1	Percent decrease in conductivity*2	Conductivity (Before)*1	Conductivity (After)*1	Percent decrease in conductivity*2
p1	2016/ 9/16–26	15,086	2016/9/20 22:00 JST	12,332	1.83	2016/9/ 20 18:00 JST	4,663	0.37	4.05 ± 0.55 (13.6%)	1.03 ± 0.34 (32.8%)	75%	4.83 ± 0.05 (1.0%)	4.72 ± 0.12 (2.5%)	2.2%
p2	2017/ 10/18–28	20,661	2017/10/23 5:00 JST	7,984	1.26	2017/10/ 23 1:00 JST	14,124	1.10	3.46 ± 0.32 (9.2%)	2.44 ± 0.75 (30.8%)	30%	4.45 ± 0.08 (1.8%)	4.15 ± 0.06 (1.4%)	6.7%
p3	2018/ 8/19–29	7,501	2018/8/24 10:00 JST	2,633	0.54	2018/8/ 24 4:00 JST	6,614	0.46	4.57 ± 0.16 (3.6%)	3.84 ± 0.59 (15.4%)	16%	4.97 ± 0.05 (0.9%)	4.96 ± 0.10 (2.1%)	0.2%
p4	2018/ 8/31–9/ 10	10,833	2018/9/5 1:00 JST	9,017	1.66	2018/9/4 19:00 JST	2,902	0.26	4.11 ± 0.28 (6.8%)	2.56 ± 0.83 (32.5%)	38%	4.90 ± 0.06 (1.3%)	4.81 ± 0.16 (3.4%)	1.9%
p5	2018/ 9/26– 10/6	13,530	2018/10/1 5:00 JST	9,288	1.36	2018/10/ 1 1:00 JST	7,581	0.56	3.33 ± 0.23 (6.8%)	2.48 ± 0.74 (30.0%)	26%	4.60 ± 0.09 (2.0%)	4.51 ± 0.16 (3.4%)	1.8%

*1 The value in the parenthesis was the coefficient of variation (CoV).

*2 Percent decrease means the ratio of the decrease in mean conductivity after river discharge peaks to that before the peaks.

$$\sigma_{2N}(\omega_{DN}) = 8\pi \int_{-\infty}^{\infty}\int_{-\infty}^{\infty} |\Gamma_{TN}|^2 S_N(m_1\mathbf{k}_{1N}) S_N(m_2\mathbf{k}_{2N}) \delta(\omega_{DN} - m_1\omega_{1N} - m_2\omega_{2N}) d\mathbf{k}_{1N} d\mathbf{k}_{2N} \quad (3)$$

where ω_{DN} and ω_{iN} are the Doppler angular frequency and wave angular frequency, respectively, normalized by the Bragg angular frequency ω_b, and $\mathbf{k}_{iN}$ is the wavenumber vector normalized by $2k_0$. m_i is the sign (± 1) determined from the range of Doppler angular frequency ω_{DN} (Hisaki 1996). $\mathbf{n}$ is the unit vector, and $S_N(m_i\mathbf{k}_{iN})$ is the normalized form of the wave spectrum for wavenumber vector $\mathbf{k}_i$, which is written as $S_N(\mathbf{k}_{1N}) = (2k_0)^4 S(\mathbf{k}_i)$. Γ_{TN} is the total coupling coefficient, which can be divided into the electromagnetic (Γ_{EN}) and hydrodynamic (Γ_{HN}) components normalized by $2k_0$ (i.e. $\Gamma_{TN} = \Gamma_{EN} - i\Gamma_{HN}$) (Hisaki 1996; Lipa and Barrick 1986) as follows:

$$\Gamma_{EN} = \frac{1}{2}\left[\frac{(\mathbf{k}_{1N}\cdot\mathbf{n})(\mathbf{k}_{2N}\cdot\mathbf{n}) - 2\mathbf{k}_{1N}\cdot\mathbf{k}_{2N}}{(\mathbf{k}_{1N}\cdot\mathbf{k}_{2N})^{1/2} - \Delta/2}\right], \quad (4)$$

$$\Gamma_{HN} = \frac{1}{2}\left\{\begin{array}{l} k_{d1N} + k_{d2N} + \frac{\mathbf{k}_{1N}\cdot\mathbf{k}_{2N} - k_{d1N}k_{d2N}}{m_1 m_2 (k_{d1N}k_{d2N})^{1/2}}\left(\frac{\omega_{DN}^2+1}{\omega_{DN}^2-1}\right) \\ + \frac{\omega_{DN}\left[m_1 k_{d1N}^{3/2}\mathrm{csch}^2(k_{1N}h_N) + m_2 k_{d2N}^{3/2}\mathrm{csch}^2(k_{2N}h_N)\right]}{\left(\omega_{DN}^2-1\right)} \end{array}\right\} \quad (5)$$

where Δ is the sea surface impedance, which is often $0.011 - 0.012i$ according to Lipa and Barrick (1986). Eq. (5) is the normalized hydrodynamic component of the coupling coefficient for shallow water while considering the effect of wave refraction (i.e. the fourth term of Eq. (5)). For deep water (i.e. $k_{iN}h_N \to \infty$), the fourth term of Eq. (5) is neglected because $\mathrm{csch}(k_{iN}h_N) \to 0$, and k_{diN} is the wavenumber for deep water, which is equal to k_{iN} when $k_{iN}h_N \to \infty$ according to the following linear dispersion relation normalized by ω_B (Hisaki 1996).

$$\omega_N^2 = k_N \tanh(k_N h_N) \quad (6)$$

Following Barrick 1977a, 1977b), H_{rms} is available from the Barrick equation derived from a ratio of the weighted second-order powers to the first-order powers.

$$H_{sr} = 4H_{rms} = 4\sqrt{\frac{2\int_{-\infty,0}^{0,\infty}\left[\frac{\sigma_{2N}(\omega_{DN})}{w(\omega_{DN})}\right]d\omega_{DN}}{k_0^2\int_{-\infty,0}^{0,\infty}\sigma_{1N}(\omega_{DN})d\omega_{DN}}} \quad (7)$$

where $w(\omega_{DN})$ is a dimensionless weighting function for each ω_{DN}, which averages the total coupling coefficient $\Gamma_{TN}$for deep water over the radar-to-wave direction (Barrick 1977a, 1977b). When calculating H_{sr} by Eq. (7), the second-order scattering is normalized by the first-order scattering peak in the same frequency domain; thus, the integral range is defined as $[-\infty, 0]$ or $[0, \infty]$.

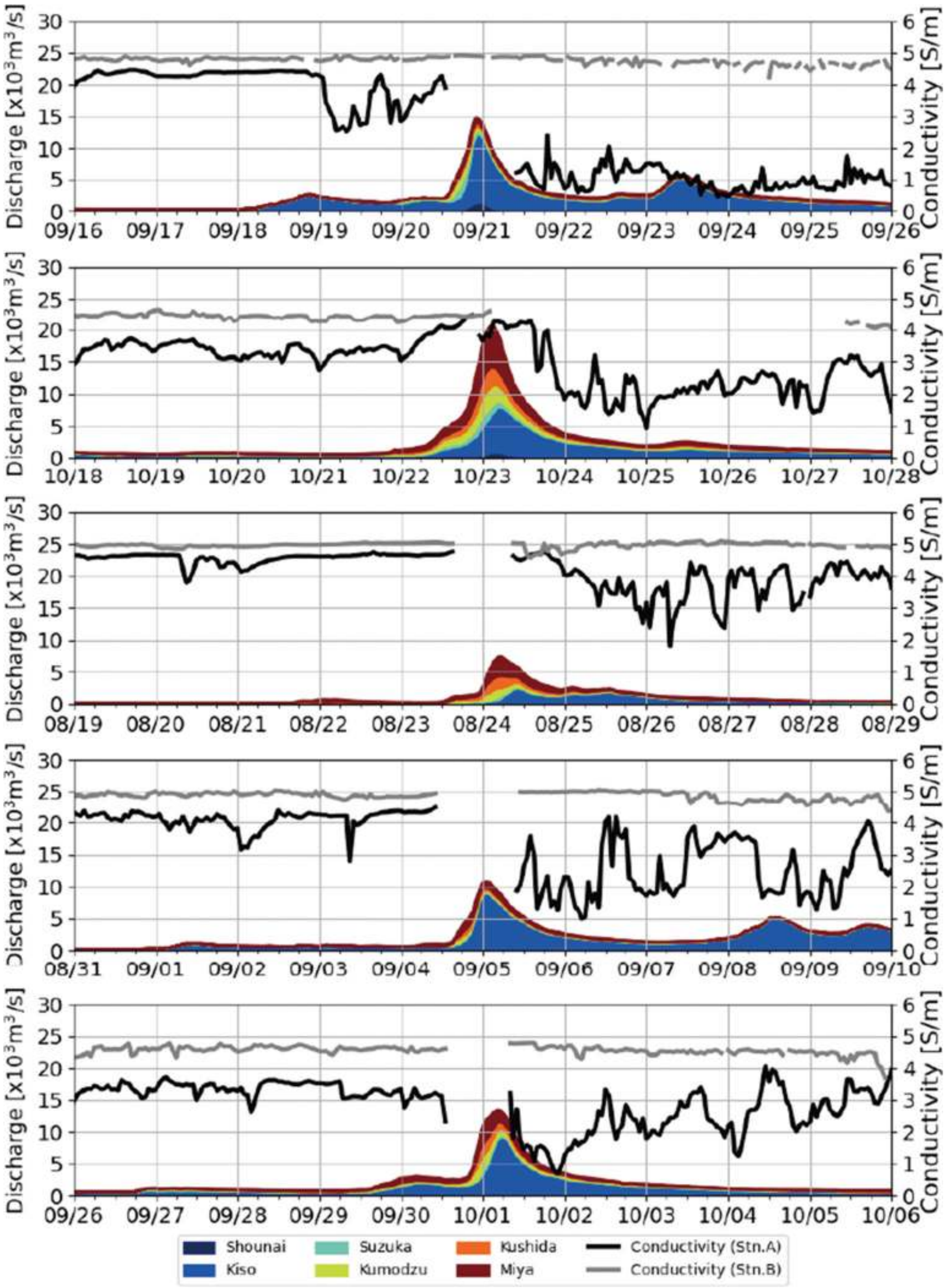

Figure 2. Time series of river discharge from each river basin and seawater conductivity. From the top, the time series in p1 to p5 are described. Notably, the river discharge in the Kiso (Suzuka) river basin is summed up by those of the Kiso, Nagara and Ibi Rivers (utsube and Suzuka Rivers). The seawater conductivity is calculated from the SSS and SST observed at Stn. A and B (see Figure 1).

2.4. Computation of significant wave height derived by the HF radar system

In the present study, H_{sr} at polar grids on beams around Stns. A and B (Figure 1) were computed by Eq (7) and were then compared with those observed by the wave gauge/buoy at both stations. A single HF radar system provided the four Doppler spectra at the polar grids around each station; thus, up to twelve Doppler spectra around them were obtained from the three HF radar systems (Figure 3). The Doppler shift induced by surface ocean currents was removed as preprocessing for extracting wave information. Furthermore, the abnormal peaks that are of about the same power as the first-order peak (mainly, ship-induced noise) were simply removed by comparing them with a smoothed Doppler spectrum in each of negative and positive frequency domains (e.g. Chuang, Chung, and Tang (2015)). Then the backscattered powers were linearly interpolated. However, since this simple removal process is not robust, several ship-derived noise remain. We discussed the negative effect of the residual noise on wave measurement in 3.1. Then, the Doppler spectrum was divided into first- and second-order scattered components by identifying the local minimum around the first-order peak. H_{sr} was computed using the first- and second-order backscattered powers in the negative and positive frequency domains of the Doppler spectrum, which means that two H_{sr} values were extracted from a single Doppler spectrum. Finally, up to 24 H_{sr} values around the 1.5-km grid point (4 polar grids/radar × 3 radars × 2 (negative and positive) frequency domains of Doppler spectrum) were extracted by applying Eq (7).

Doppler spectra that do not follow Barrick's theory should be discarded in advance to avoid incorrectly estimating wave heights. Thus, the Doppler spectra with $\mathrm{SNR}_2 \leq 10$ dB were removed according to Wyatt (2005) when extracting H_{sr} (Figure 3). SNR_2 was evaluated using the second-order peak in the outer band of each frequency domain against a noise floor level in the same domain. The noise floor level was determined by averaging the noise power over the outer edge of each domain (i.e. $1.79 < |\omega_{DN}| < 1.94$) beyond 60 km from each radar station at each time point. Note that the noise floor levels were defined from a range-Doppler map but not from a single Doppler spectrum. This removes the effect of wave-induced powers and/or local external noises from the noise floor level. Furthermore, SNR_1 was also computed with the ratio of the first-order peak to the noise floor level in each domain to assess the capability as a criterion for the wave spectrum inversion.

2.5. Statistical analysis

The HF radar-derived significant wave height (H_{sr}) was compared with that measured by the wave gauge/buoy (H_{so}). The measurement accuracy was evaluated with four indexes, that is, Pearson's correlation coefficient (r), *bias*, root mean square error (*RMSE*) without bias, and scatter index (*SI*), as follows.

$$r = \frac{\sum (H_{so} - \langle H_{so} \rangle)(H_{sr} - \langle H_{sr} \rangle)}{\sqrt{\sum (H_{so} - \langle H_{so} \rangle)^2} \sqrt{\sum (H_{sr} - \langle H_{sr} \rangle)^2}} \tag{8}$$

$$bias = |\langle H_{sr} \rangle - \langle H_{so} \rangle| \tag{9}$$

$$RMSE = \sqrt{\frac{1}{N} \sum (H_{sr} - H_{so} - bias)^2} \tag{10}$$

$$SI = RMSE / \langle H_{so} \rangle \tag{11}$$

where $\langle H_{sr} \rangle$ and $\langle H_{so} \rangle$ are the temporal averages during each computing period for comparison, and N denotes the amount of data. The python package "scipy (ver 1.4.1)" was used in the statistical analysis.

Furthermore, Pearson's correlation coefficient was also adopted to discuss the effect of environmental factors (freshwater inflow volume, seawater conductivity) on the measurement accuracies (i.e. Eq (9) and Eq (11)) and was then tested with a 95% confidence level using a t test.

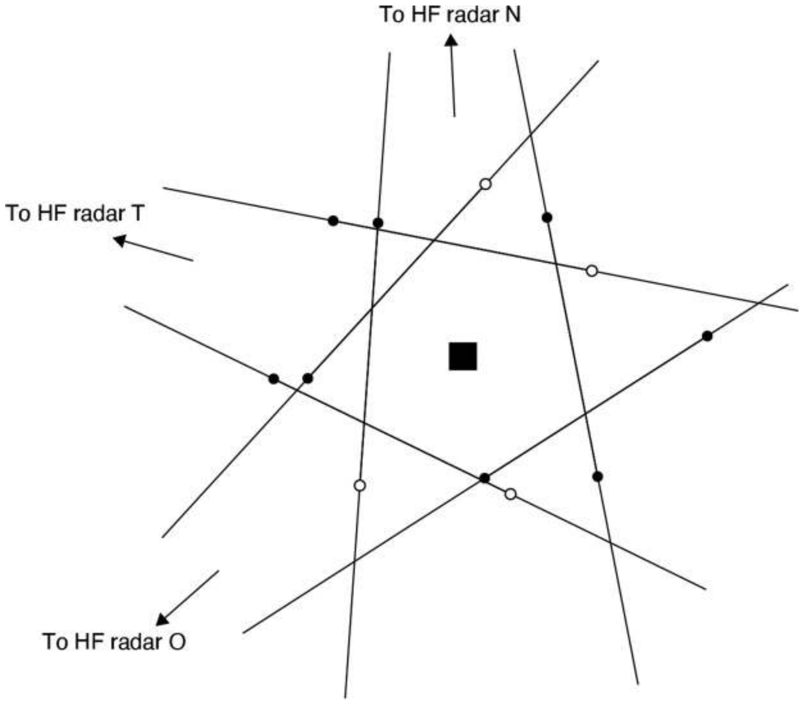

Figure 3. Schematic image of the selection of Doppler spectra to extract significant wave heights. The filled (white) circles indicate the parallel grid point at which the Doppler spectrum with SNR_2 >10 dB (SNR_2 ≤10 dB) is observed. The square indicates the 1.5-km grid point at which the significant wave height is calculated. In this case, the eight Doppler spectra are utilized to compute the significant wave height.

3. Results and discussion

3.1. Extraction of significant wave height from Doppler spectra in Ise Bay

Up to 24 H_{sr} values were computed at each time by Eq (7) and then compared with H_{so} values at Stns. A and B during the five periods (Figure 4). Overall, H_{sr} greatly fluctuated against H_{so}. A possible cause of the large fluctuation in H_{sr} could be the decline in SNR_2 and/or the occurrence of unexpected peaks in the second-order domain. These unexpected peaks occur due to various factors. One factor is temporary obstructions in the working range of the HF radar (e.g. ship) (Maresca et al. 2011). Many ships operate in Ise Bay because of activity in the Ports of Nagoya and Yokkaichi, with more than 50,000 domestic/international ships entering Ise Bay each year as well as fishery ships that operate in the bay. The strong ship-derived echoes contaminate the Doppler spectrum. Another factor is radio interference, which can have a major impact on the performance of HF radar measurements (Gurgel, Barbin, and Schlick 2007). In Ise Bay, the operation times of the three radar systems were shifted by 10 min to avoid interference among these systems (see 2.2); however, several unexpected echoes induced by radio interference were confirmed, especially radar N. These echoes in the Doppler spectrum extended over a measurable distance from the radar station. These unexpected peaks would yield an overestimation of H_{sr}.

Interestingly, the minima among the estimated H_{sr} ($H_{sr,min}$) values at Stn. B were relatively consistent with H_{so} (black solid line in Figure 4), although several abnormal variabilities were observed ($n = 1200$, $r = 0.71$, $bias = 0.18$ m, $SI = 0.82$; see Table 2). In contrast, $H_{sr,min}$ at Stn. A greatly fluctuated against H_{so} ($n = 1184$, $r = -0.01$, $bias = 1.23$ m, $SI = 6.45$; see Table 2); in particular, the accuracy of $H_{sr,min}$ worsened after peak river discharge (arrows of each panel in Figure 4). The temporal variability of $H_{sr,min}$ before the peak was relatively consistent with that of H_{so} at Stn. A as well as Stn. B (Stn. A: $n = 610$, $r = 0.74$, $bias = 0.28$ m, $SI = 0.83$; Stn. B: $n = 611$, $r = 0.85$, $bias = 0.11$ m, $SI = 0.53$; see Table 2). The correlation between H_{so} and H_{sr} at each radar station before the river discharge peak is shown in Figure 5. Basically, H_{sr} was overestimated against H_{so} (Figure 5), while $H_{sr,min}$ was relatively correlated with H_{so}. $H_{sr,min}$ values at Stns. A and B were often extracted from radar N (Stn. A – radar N: 11.1 km; Figure 5a) and radar O (Stn. B – radar O: 18 km; Figure 5f) depending on the distance from the radar stations. The accuracy of $H_{sr,min}$ at Stn. A deteriorated compared with Stn. B (Figure 5) regardless of whether the monitoring site was closer to the radar station (Figure 1).

3.2. Decrease in wave measurement accuracy due to freshwater inflow

A possible cause for a decrease in the accuracy at Stn. A is the attenuation of HF radio waves due to seawater desalination induced by the freshwater inflow (Gurgel, Essen, and Kingsley 1999). Seawater desalination yields a decline in seawater conductivity and thus results in a reduction in SNRs (Gurgel, Essen, and Kingsley 1999; Forget and Broche 1991). In fact, the seawater conductivity around Stn. A showed dramatic changes due to the freshwater inflow (Figure 2) because Stn. A was close to the mouth of the Kiso River, which is the largest river in the Ise Bay basin (Figures 1 and 2). In contrast, the conductivity at Stn. B slightly changed. As expected, the mean conductivity at Stn. A after the river discharge peak significantly decreased between 16% and 75%, yielding a larger variance in the conductivity, while that at Stn. B was only a 0.2% to 6.7% decrease with a smaller variance (Table 1). The percent decrease in mean conductivity at Stn. A (Stn. B) was the largest in p1 (p2), resulting from the large river discharge from the northern (western) part of the bay (Table 1). In fact, the percent decrease in mean conductivity at Stn. A strongly correlated with the freshwater inflow volume from the northern rivers ($n = 5$, $r = 0.801$, $p = 0.103$), whereas the decrease at Stn. B strongly correlated with the volume from western rivers ($n = 5$, $r = 0.853$, $p = 0.066$). Unfortunately, a statistically significant correlation at the 95% confidence level was not found because of a few data points (i.e. $n = 5$). However, in contrast to these correlations, the relationship of the percent decrease at Stn. A (Stn. B) with freshwater volume from western (northern) rivers was weak ($n = 5$, $r = 0.320$, $p = 0.600$ for percent decrease at Stn. A vs. freshwater volume from western rivers; $n = 5$, $r = 0.240$, $p = 0.697$ for percent decrease at Stn. B vs. freshwater volume from northern rivers). These results suggest that the freshwater inflow from northern and western rivers leads to the decrease in seawater conductivity at Stns. A and B, respectively.

The percent decrease in mean seawater conductivity determined the wave measurement accuracy. Comparing *bias* and *SI* for each period at Stns. A and B (Table 2) with the percent decrease (Table 1), the percent decrease at Stn. A showed a statistically significant correlation with both *bias* and *SI* ($n = 5$, $r = 0.970$, $p < 0.01$ for *bias*; $n = 5$, $r = 0.971$, $p < 0.01$ for *SI*), but a significant correlation at Stn. B was not found ($n = 5$, $r = 0.133$, $p = 0.832$ for *bias*; $n = 5$, $r = 0.090$, $p = 0.886$ for *SI*). This verifies the deterioration of wave measurement accuracy at Stn. A caused by the decrease in seawater conductivity, as the measurement accuracy at Stn. B was not always dependent on conductivity. This is because the attenuation pattern of radio waves at a distance from a radar station

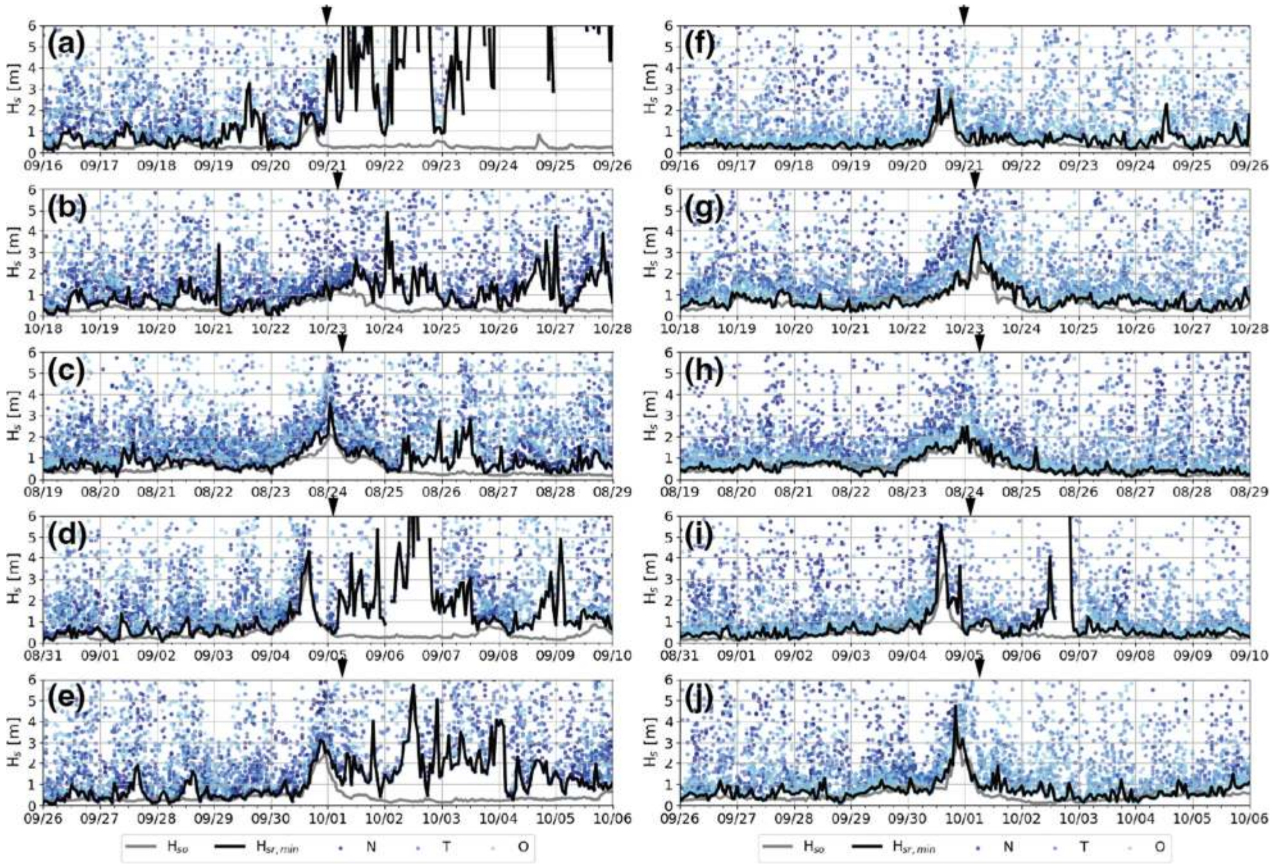

Figure 4. Time series of significant wave heights extracted from the Doppler spectra. The color dots indicate H_{sr} estimated from up to 24 Doppler spectra. The black solid line indicates $H_{sr,min}$ among up to 24 H_{sr}, and the gray solid line indicates H_{so} observed by wave gauge/buoy. The arrow on the upper edge of each panel denotes the time at which the peak of total river discharge occurred (see Figure 2). From the top, the time series in p1 to p5 are described. The left and right panels are the time series at Stns. A and B, respectively.

Table 2. Accuracy of $H_{sr,min}$ in total duration and only before the river discharge peak.

		Stn. A				Stn. B			
	Period	*bias* [m]	*SI*	*r*	*n*	*bias* [m]	*SI*	*r*	*n*
Total duration	p1	3.52	16.49	−0.08	226	0.20	0.81	0.72	241
	p2	0.65	1.98	0.11	241	0.16	0.55	0.79	241
	p3	0.38	0.87	0.58	241	0.07	0.37	0.87	241
	p4	0.88	3.19	0.15	235	0.28	1.54	0.63	236
	p5	0.84	2.60	0.17	241	0.20	0.65	0.77	241
	All	1.23	6.45	−0.01	1184	0.18	0.82	0.71	1200
Only before river discharge peak	p1	0.40	1.60	0.34	118	0.11	0.53	0.91	118
	p2	0.30	1.10	0.29	123	0.01	0.32	0.81	123
	p3	0.24	0.45	0.86	125	0.03	0.27	0.90	125
	p4	0.20	0.51	0.92	120	0.22	0.88	0.88	121
	p5	0.24	0.76	0.84	124	0.17	0.55	0.85	124
	All	0.28	0.83	0.74	610	0.11	0.53	0.85	611

affects the signal level in the far zone (Forget and Broche 1991). Even if the conductivity at a target point was high, the radio waves could be highly attenuated in the low-conductivity region, which is close to a radar station such as Stn. N (Figure 1).

3.3. Requirement of signal-to-noise ratio (SNR) for wave measurement

Here, a question arises: How should we select the Doppler spectra to extract ocean wave information? As mentioned above, the minimum value among the estimated significant wave heights (i.e. $H_{sr,min}$) before flooding was relatively consistent with H_{so} (Figure 4). This implies that various noises yielded unexpected peaks in the second-order frequency domain and thus basically worked toward the overestimation of H_{sr} (Figure 5). To answer the above question, we consider a criterion for selecting the Doppler spectra for wave measurement.

In the present study, SNR_1 and SNR_2 were considered criteria for wave measurement. To examine the requirements of SNR_1 and SNR_2, relative errors (RE) in all periods were computed by $\left|H_{sr,min} - H_{so}\right|/H_{so}$. Note that SNR_1 and SNR_2 were evaluated in the positive/negative domain

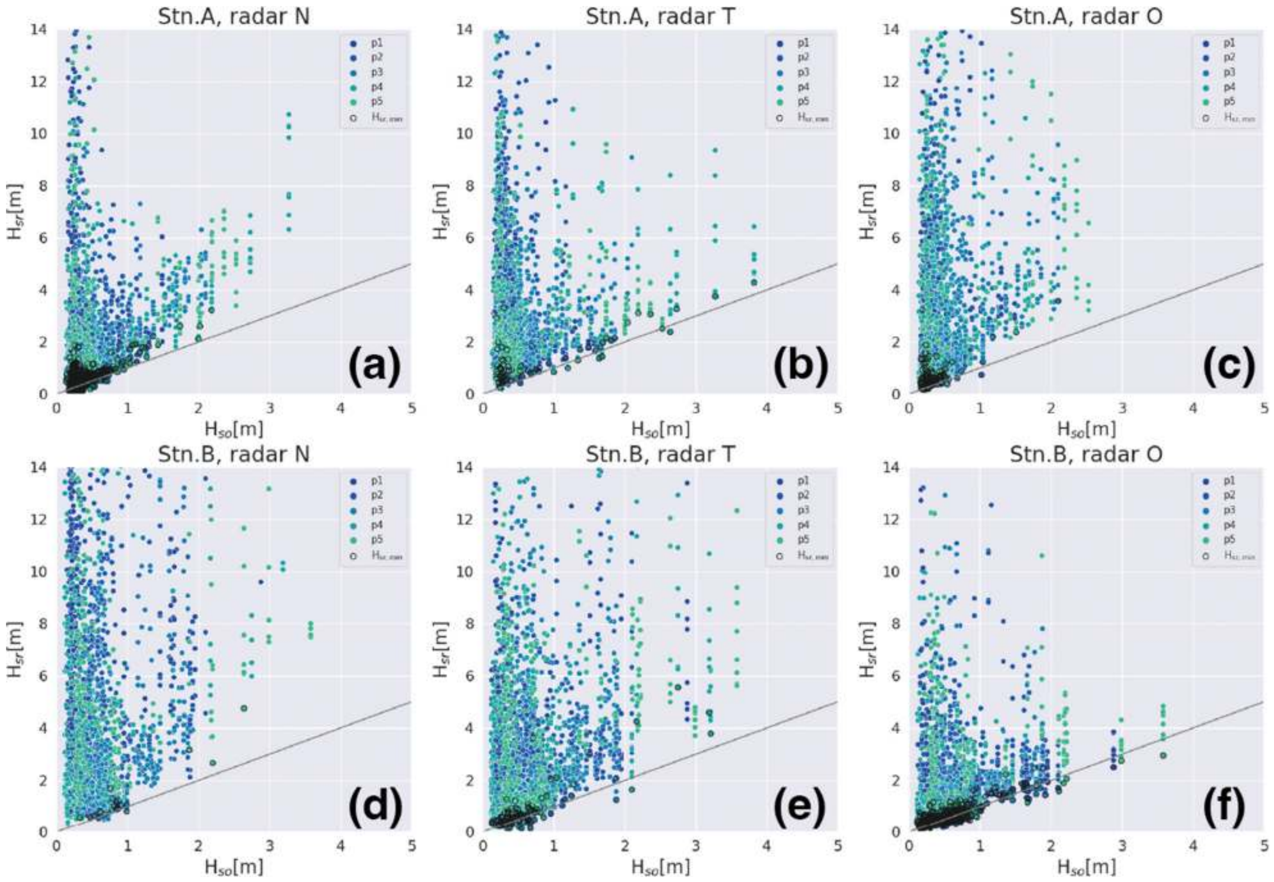

Figure 5. Comparison between the significant wave heights estimated by applying the Doppler spectrum observed by three radar systems to Barrick's equation (H_{sr}) and observed by wave gauge/buoy (H_{so}) in the duration before the river discharge peak. The upper and lower panels denote the scatter plots at Stns. A and B, and the left, center and right panels denote those from radar N, T and O, respectively. The colors show the calculation periods, and the outlined circles show the minima of H_{sr} ($H_{sr,min}$). Their legend is shown in the upper right of each panel.

from which $H_{sr,min}$ was computed. Figure 6 shows a two-dimensional density plot in the SNR_1-SNR_2 plane when RE < 50% (Figure 6a and b) and RE > 50% (Figure 6c and d). The acquisition rate of $H_{sr,min}$ with RE < 50% at Stn. B was 60%, which was higher than that at Stn. A (33%) (Figure 2). $H_{sr,min}$ with RE < 50% at both sites was likely to be available with SNR_1 >40 dB (Figure 6a and b). In the case of RE > 50%, SNR_1 at Stn. A was less than 40 dB (Figure 6c), while SNR_1 at Stn. B was greater than 40 dB (Figure 6d). The deterioration of $H_{sr,min}$ at Stn. B was seen even if SNR_1 >40 dB (Figures 6d). The density plots also indicate that wave measurement requires an SNR_2 of at least 10 dB, which is consistent with Wyatt et al. (2005) (Figure 6a and b). On the other hand, $H_{sr,min}$ with RE > 50% was often estimated at Stn. B even if SNR_2 >10 dB. This implies that such a higher SNR_2 would be derived from not only wave-induced echoes but also noise-induced echoes which were unrelated to Barrick's theory.

3.4. Capability of the wave height estimated by Barrick's equation as a criterion for nonlinear inversion of ocean wave spectrum

Based on these results, we formulated a hypothesis that H_{sr} is helpful in selecting the Doppler spectrum with low contamination by noise when applying an inversion of the wave spectrum. This idea was originated by Hisaki (2015), but its capability was not sufficiently validated. Furthermore, the applicability of wave measurements in estuary regions such as Ise Bay is unknown. As a method of wave spectrum inversion, the BIM for shallow water established by Kataoka and Nagamatsu (2016) was applied, which is modified from the BIM for deep water originally proposed by Hashimoto and Tokuda (1999), as concisely described in Appendix A.

To demonstrate the hypothesis, we compared three algorithms with different criteria for selecting the Doppler spectra in the BIM. The first criterion was H_{sr} ($BIM_{Barrick}$), and the second and third criteria were SNR_1 (BIM_{SNR1}) and SNR_2 (BIM_{SNR2}), respectively. In $BIM_{Barrick}$, the Doppler spectra were used when the relative difference of up to 24 H_{sr} against $H_{sr,min}$ (i.e. $\left|H_{sr} - H_{sr,min}\right|/H_{sr,min}$) was lower than 50% ($BIM_{Barrick}$). Meanwhile, the Doppler spectra in BIM_{SNR1} and BIM_{SNR2} were selected when SNR_1 and SNR_2 in the Doppler frequency domain with the strongest first-order peak were greater than 40 dB and 10 dB, respectively. Hereinafter, these quality controls before applying BIM are referred to as "prior quality control." The significant wave height (H_s) was computed by Eq (A8) using the inverted wave spectrum. Then, as "posterior quality control," the abnormal wave heights estimated by the three algorithms were neglected if $\left|H_s - H_{sr,min}\right|/H_{sr,min} > 50\%$. Finally, the acquisition rate was evaluated by a ratio of the number of H_s with RE < 50% to the total data.

The measurement accuracy of H_s was evaluated in the durations before the river discharge peaks (Table 3). For reference, the measurement accuracies of $H_{sr,min}$ are also described in Table 3. At Stn. A, H_s estimated by $\mathrm{BIM_{Barrick}}$ was more accurate than the others. At Stn. B, there were no significant differences in measurement accuracy among the three algorithms. However, we found that the acquisition rates of $\mathrm{BIM_{Barrick}}$ (Stn. A: 89%; Stn. B: 96%) were significantly higher than those of $\mathrm{BIM_{SNR1}}$ (Stn. A: 75%; Stn. B: 74%) and $\mathrm{BIM_{SNR2}}$ (Stn. A: 56%; Stn. B: 67%). This indicates that prior quality control using $\mathrm{SNR_1}$ and $\mathrm{SNR_2}$ frequently caused the occurrence of abnormal wave heights (i.e. $\left|H_s - H_{sr,min}\right|/H_{sr,min} > 50\%$) due to the presence of non-wave signals in the Doppler spectra.

H_{sr} was a functional criterion for the prior quality control. For example, Figure 7 shows the Doppler spectra around Stn. B at 13:00 JST on August 21 2018. Initially, a Doppler spectrum (Figure 7b) was rejected because $\mathrm{SNR_2} \leq 10$ dB (see 2.4), and thus, the eleven Doppler spectra with $\mathrm{SNR_2} > 10$ dB observed by three radar systems were used for $\mathrm{BIM_{SNR2}}$. The three Doppler spectra with $\mathrm{SNR_2} \leq 40$ dB (Figure 7a, c, d) were rejected for $\mathrm{BIM_{SNR1}}$, and furthermore, three Doppler spectra (Figure 7e, f, h) with $\left|H_{sr} - H_{sr,min}\right|/H_{sr,min} > 50\%$ where $H_{sr,min} = 0.82m$ (see Figure 7i) were rejected for $\mathrm{BIM_{Barrick}}$. Based on the prior quality control, the wave spectra were

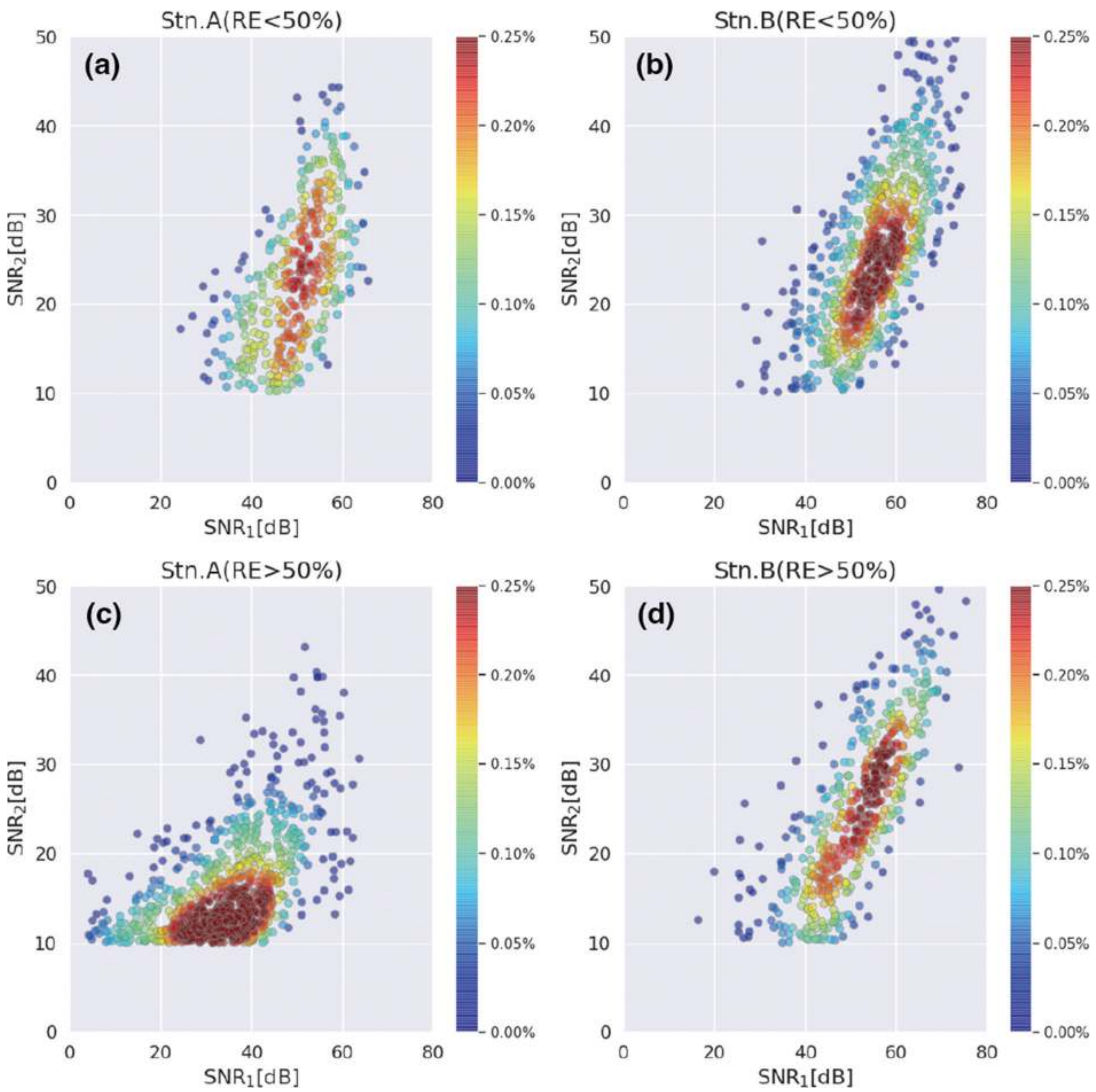

Figure 6. Two-dimensional density plot in the SNR1—SNR2 plane at Stn. A ((a) RE < 50%, (c) RE > 50%) and Stn. B ((b) RE < 50%, (d) RE > 50%).

Table 3. Comparison of measurement accuracies of significant wave height estimated by Barrick's equation ($H_{sr,min}$) and BIMs with three types of criteria ($\mathrm{BIM_{Barrick}}$, $\mathrm{BIM_{SNR1}}$, and $\mathrm{BIM_{SNR2}}$.).

	bias [m]	*RMSE* [m]	*SI* [%]	*r*	*n*	Acquisition rate [%]
$H_{sr,min}$						
Stn. A	0.28	0.38	0.83	0.74	610	100%
Stn. B	0.11	0.31	0.53	0.85	611	100%
H_s estimated by $\mathrm{BIM_{Barrick}}$						
Stn. A	0.03	0.31	0.66	0.72	545	89%
Stn. B	0.15	0.32	0.54	0.74	584	96%
H_s estimated by $\mathrm{BIM_{SNR1}}$						
Stn. A	0.09	0.37	0.76	0.60	459	75%
Stn. B	0.06	0.30	0.48	0.74	450	74%
H_s estimated by $\mathrm{BIM_{SNR2}}$						
Stn. A	0.21	0.40	0.78	0.59	340	56%
Stn. B	0.01	0.35	0.56	0.79	411	67%

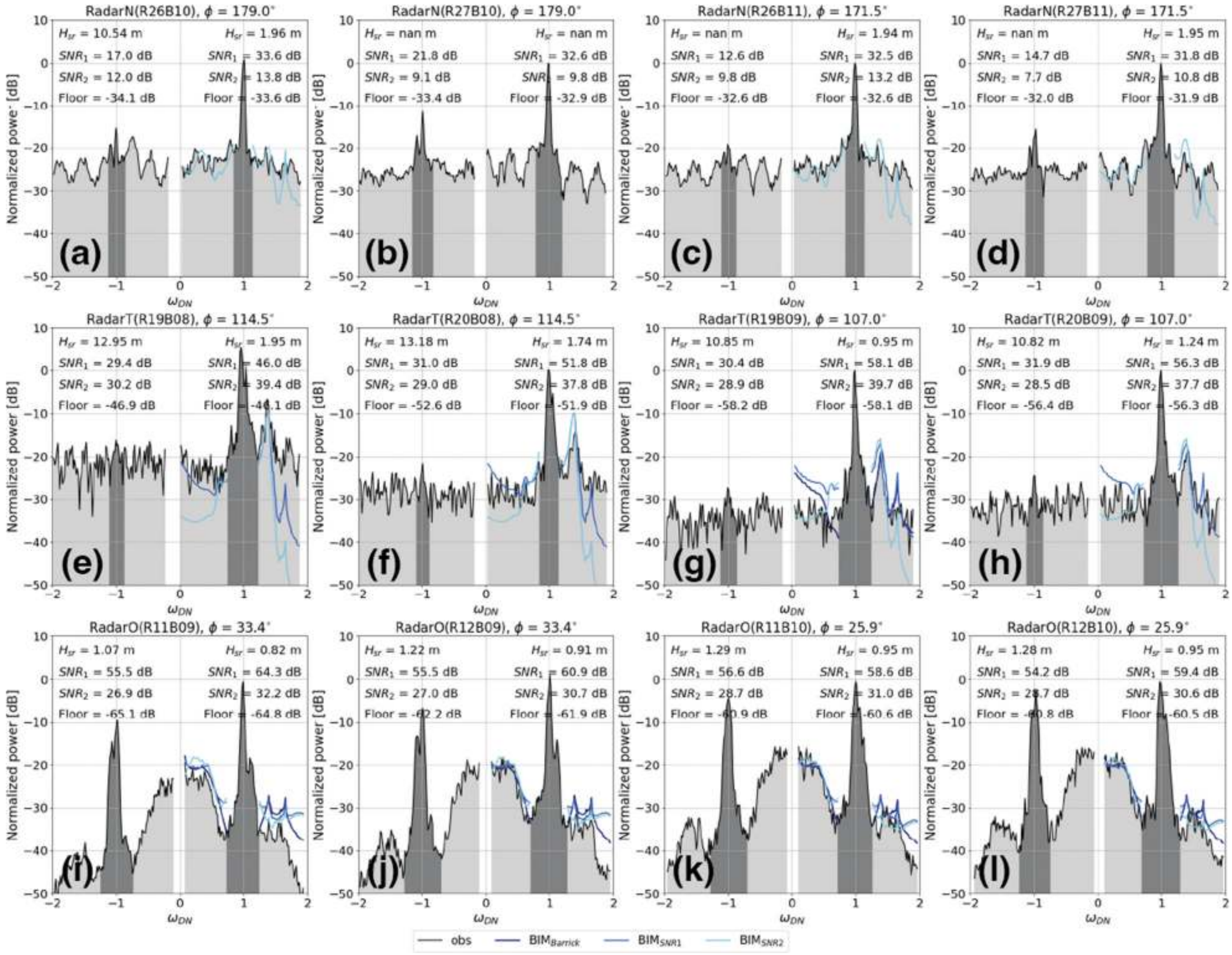

Figure 7. Example of the normalized Doppler spectra observed around Stn. B (13:00 JST, 21 August 2018). The Doppler spectra are normalized by the first-order peaks. The upper, middle and lower panels are for radar N, T and O, and the four columns are for the four polar grids. The title of each panel describes the radar station, cell number of range and beam directions and beam angle ϕ clockwise from the north. H_{sr}, $\mathrm{SNR_1}$, $\mathrm{SNR_2}$ and normalized noise floor level, which were evaluated in the positive/negative frequency domain, are described in each panel. Note that the noise floor level is also normalized by the first-order peaks to be consistent with the normalized Doppler spectra. The gray and light gray areas denote the first-order and second-order domains, respectively. The blue lines show the normalized Doppler spectrum computed from the optimum solution of ocean wave spectra inverted by $\mathrm{BIM_{Barrick}}$, $\mathrm{BIM_{SNR1}}$, and $\mathrm{BIM_{SNR2}}$ described in Figure 8, whose legends are shown in the bottom box.

estimated using the five Doppler spectra for $\mathrm{BIM_{Barrick}}$, the eight for $\mathrm{BIM_{SNR1}}$ and the eleven for $\mathrm{BIM_{SNR2}}$ (Figure 8). The wave spectra estimated by the three BIMs show that the wind waves predominantly came from the southeast, which is consistent with the wind direction observed at Stn. B, that is, southwesterly winds (135°Clockwise from the north). The significant wave height computed by $\mathrm{BIM_{Barrick}}$ ($H_s = 0.58$ m, $\mathrm{RE} = 19\%$) was reasonable with the observed height at Stn. B ($H_{so} = 0.72$ m) compared

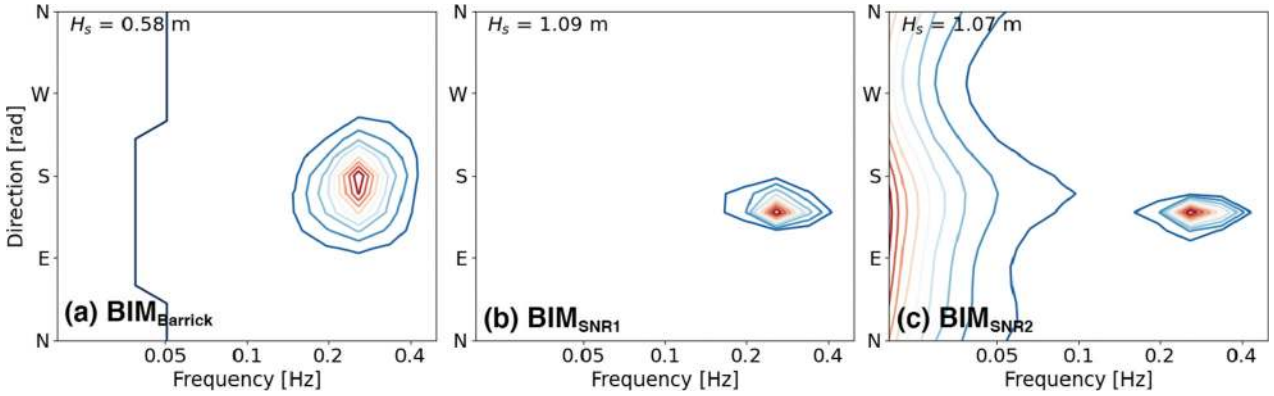

Figure 8. Example of the ocean wave spectra inverted by BIM$_{Barrick}$, BIM$_{SNR1}$, and BIM$_{SNR2}$ at Stn. B at 13:00 JST, 21 October 2018. The Doppler spectra selected in the three BIMs are described in Figure 7. The significant wave heights computed from the inverted spectrum are shown at the upper-left of each panel.

to H_s computed by BIM$_{SNR1}$ ($H_s = 1.09$ m, RE = 51%) and BIM$_{SNR2}$ ($H_s = 1.13$ m, RE = 57%). BIM$_{SNR2}$ estimated high wave energies at low frequencies (Figure 8c). The six Doppler spectra with SNR$_2$ >10 dB (Figure 7a, c, d, e, f, h) caused the overestimation of H_s compared to H_{so}. The criteria suggested by Wyatt et al. (2006) (SNR$_2$ >15 dB) can reject three of those spectra (Figure 7a, c, d), which was consistent with the SNR$_1$-based selection, whereas it was difficult to reject the remaining Doppler spectra. They were successfully rejected by using H_{sr} as the prior quality control in BIM$_{Barrick}$. This demonstrates that H_{sr} effectively functions as a criterion to reject inappropriate Doppler spectra in the BIM.

3.5. Suggestion of a methodology for providing reliable HF radar-derived wave data in the estuary region

We summarize a methodology for providing reliable HF radar-derived wave data in an estuary region. The most specific issue in this region is the attenuation of radio waves propagating on the sea surface due to the decline in seawater conductivity induced by freshwater inflow (Figure 2). Accordingly, both SNR$_1$ and SNR$_2$ significantly decreased after the river discharge peak corresponding to seawater conductivity, which yielded a deterioration in the measurement accuracy of $H_{sr,min}$ (Figure 4). HF radar-derived wave data are unavailable under seawater desalination, which is a limitation of HF radar-derived wave observations (Gurgel, Essen, and Kingsley 1999).

Nevertheless, further research is necessary to define the threshold values of the conductivity because the attenuation of radio waves is dependent on the distance from the radar station and radio frequency as well (Gurgel, Essen, and Kingsley 1999; Toguchi and Fujii 2023). Figure 9 shows the dependence of the RE of H_s estimated by BIM$_{Barrick}$ on the conductivity. At Stn. B with the higher conductivity (mostly conductivity >4 S/m), the acquisition rate of H_s (percentage of RE < 50% in the total number) was 67%. On the other hand, the acquisition rate at Stn. A with the lower conductivity significantly decreased depending on the deterioration of the conductivity (Figure 9), but the acquisition rate at Stn. A (71%) was slightly greater than that at Stn. B (67%) when the conductivity >4 S/m because of the shorter distance from the radar station. Moreover, even if the conductivity ranged between 3 and 4 S/m at Stn. A, the acquisition rate of H_s was 52%.

In addition, the first-order and second-order Doppler spectra in the bay were often contaminated by other external noises. This noise occurs in the non-wave-induced peaks in those frequency domains, which could overestimate SNR$_1$ and SNR$_2$. Although SNR$_1$ and SNR$_2$ are important criteria to evaluate the quality of Doppler spectra, these criteria could not select the appropriate Doppler spectra for the wave spectrum inversion in the bay (see 3.4).

Here, our suggestion is to employ H_{sr} as the criterion for the inversion. The present study demonstrates that H_{sr} could select adequate Doppler spectra from those affected by desalination and containing noise. Consequently, the wave measurement accuracy and acquisition rates of the BIM$_{Barrick}$-derived H_s were improved compared with those of BIM$_{SNR1}$ and BIM$_{SNR2}$ (Table 3). Although the present study only focused on the significant wave height, we need to further validate other wave parameters, such as wave period and direction. Additionally, it is necessary to consider the applicability of the suggestion listed in the present study in other estuary regions and radar systems with different radio frequencies.

4. Summary

To explore the applicability of high-frequency (HF) radar systems in estuary regions for wave measurement, we validated the significant wave height in Ise Bay, Japan, by applying a traditional equation

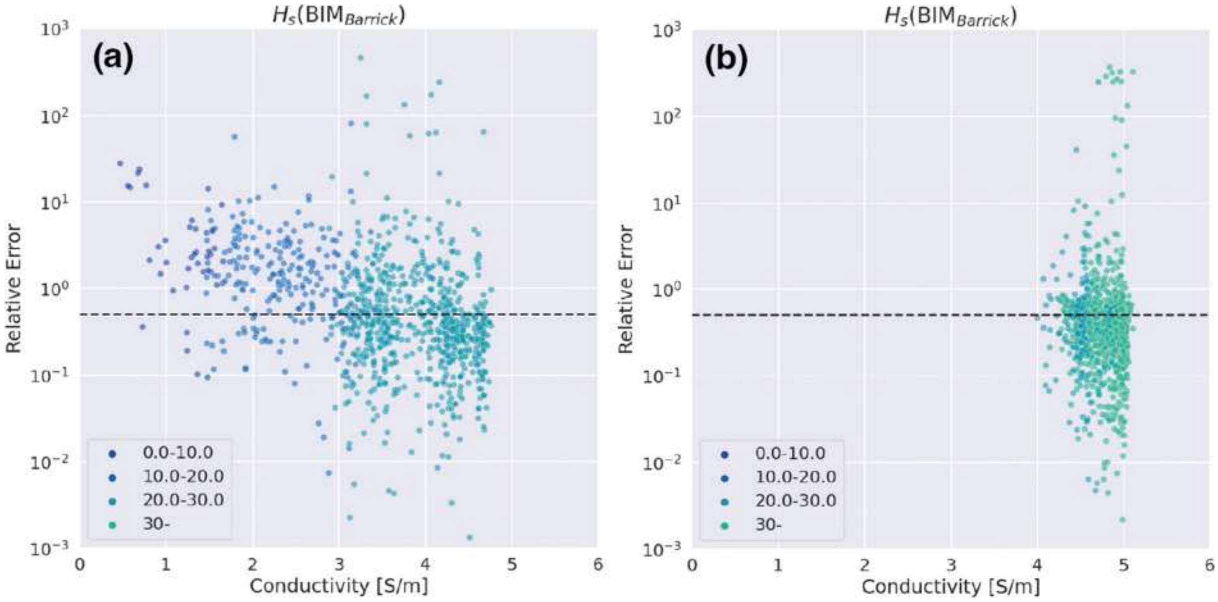

Figure 9. Relationship between the relative error (RE) of the estimated significant wave height and seawater conductivity at Stns. A and B. RE was evaluated by comparing the significant wave heights estimated by BIM$_{Barrick}$ with the observed heights at Stns. A (a) and B (b). The color denotes sea surface salinity (SSS); a legend is shown at the lower left of each panel. The horizontal broken line indicates RE = 50%, which was used as a threshold value of RE in the present study.

formulated by Barrick (1977a) and then assessing the deterioration of the measurement accuracy of the wave height and factors that influence it. Moreover, the capability of using the wave height derived by the Barrick equation in a nonlinear inversion for the two-dimensional wave spectrum from Doppler spectra was considered.

The minimum ($H_{sr,min}$) of up to 24 significant wave heights computed by the Barrick equation to the Doppler spectra observed by three radar systems around a 1.5-km regular grid point was consistent with the wave height measured by wave gauges/buoys at two sites (Stns. A and B) in the bay. The measurement accuracy at Stn. A, which was close to the mouth of the major rivers, notably deteriorated due to the decrease in seawater conductivity from the inflow of freshwater, as indicated by the significant correlation between the accuracy indexes (*bias* and *SI*) and the percent decrease in the conductivity.

Furthermore, the requirement for wave measurement was assessed by computing the signal-to-noise ratios of the first-order (SNR$_1$) and second-order peaks (SNR$_2$) against a noise floor level. The significant wave height at Stn. A tended to be accurately measured when SNR$_1$ >40 dB, while that at Stn. B deteriorated even if SNR$_1$ >40 dB. In addition, there were no significant differences in SNR$_2$. These results highlight the difficulty in determining the threshold values of SNR$_1$ and SNR$_2$ for measuring ocean waves in estuary regions.

To explore more suitable criteria for wave measurement in estuary regions, nonlinear inversion methods using H_{sr} (BIM$_{Barrick}$), SNR$_1$ (BIM$_{SNR1}$), and SNR$_2$ (BIM$_{SNR2}$) were applied. BIM$_{Barrick}$ successfully selected appropriate Doppler spectra, whereas BIM$_{SNR1}$ and BIM$_{SNR2}$ had difficulty selecting the Doppler spectrum observed in the estuary due to desalination and noise contamination. Consequently, BIM$_{Barrick}$ showed better performance than BIM$_{SNR1}$ and BIM$_{SNR2}$ in terms of a high acquisition rate, although there was difficulty in determining the best method in terms of measurement accuracy. Therefore, our results demonstrate that H_{sr} can select appropriate Doppler spectra from those deteriorated in the estuary regions.

Acknowledgments

We are grateful to the Ministry of Land, Infrastructure, Transport and Tourism, Japan (MLIT), for providing the Doppler spectrum data, wave data stored in NOWPHAS and water quality data observed in Ise Bay. And we would like to thank American Journal Experts (https://www.aje.com/) for English language editing with high quality, and also thank anonymous reviewers for their comments to improve the manuscript.

Disclosure statement

No potential conflict of interest was reported by the author(s).

Funding

The work was supported by the Japan Society for the Promotion of Science [20KK0093].

ORCID

Tomoya Kataoka http://orcid.org/0000-0002-2921-8041
Takashi Fujiki http://orcid.org/0000-0001-8415-3087

References

Akaike, Hirotugu. 1980. “Likelihood and the Bayes Procedure.” *Trabajos de Estadistica Y de Investigacion Operativa* 31 (1): 143–166. https://doi.org/10.1007/BF02888350.

Barrick, D. E. 1971. “Theory of HF and VHF Propagation Across the Rough Sea, 1, the Effective Surface Impedance for a Slightly Rough Highly Conducting Medium at Grazing Incidence.” *Radio Science* 6 (5): 517–526. https://doi.org/10.1029/RS006i005p00517.

Barrick, D. E. 1972a. Remote Sensing of Sea State by Radar. Paper presented at the Ocean 72 - IEEE International Conference on Engineering in the Ocean Environment, Newport, Rhode Island, USA, September 13–15, 1972. https://ieeexplore.ieee.org/document/1161166

Barrick, D. E. 1977a. “Extraction of Wave Parameters from Measured HF Radar Sea-Echo Doppler Spectra.” *Radio Science* 12 (3): 415–424. https://doi.org/10.1029/RS012i003p00415.

Barrick, D. E. 1977b. “The Ocean Waveheight Nondirectional Spectrum from Inversion of the HF Sea-Echo Doppler Spectrum.” *Remote Sensing of Environment* 6 (3): 201–227. https://doi.org/10.1016/0034-4257(77)90004-9.

Barrick, Donald E. 1972b. “First-Order Theory and Analysis of MF/HF/VHF Scatter from the Sea.” *IEEE Transactions on Antennas & Propagation* 20 (1): 2–10. https://doi.org/10.1109/TAP.1972.1140123.

Barrick, D. E., and B. L. Weber. 1977. “On the Nonlinear Theory for Gravity Waves on the Ocean’s Surface. Part II: Interpretation and Applications.” *Journal of Physical Oceanography* 7 (1): 11–21. https://doi.org/10.1175/1520-0485(1977)007<0011:OTNTFG>2.0.CO;2.

Chuang, L. Z. H., Y. J. Chung, and S. T. Tang. 2015. “A Simple Ship Echo Identification Procedure with SeaSonde HF Radar.” *IEEE Geoscience & Remote Sensing Letters* 12 (12): 2491–2495. https://doi.org/10.1109/LGRS.2015.2487363.

Crombie, Douglass D. 1955. “Doppler Spectrum of Sea Echo at 13.56 Mc./S.” *Nature* 175 (4459): 681–682. https://doi.org/10.1038/175681a0.

Forget, P., and P. Broche. 1991. “A Study of VHF Radio Wave Propagation Over a Water Surface of Variable Conductivity.” *Radio Science* 26 (5): 1229–1237. https://doi.org/10.1029/91RS01413.

Green, J. J., and L. R. Wyatt. 2006. “Row-Action Inversion of the Barrick-Weber Equations.” *Journal of Atmospheric and Oceanic Technology* 23 (3): 501–510. https://doi.org/10.1175/JTECH1854.1.

Guiomar, Lopez, and Daniel C. Conley. 2019. “Comparison of HF Radar Fields of Directional Wave Spectra Against In Situ Measurements at Multiple Locations.” *Journal of Marine Science and Engineering* 7 (8). https://doi.org/10.3390/jmse7080271.

Gurgel, K., Y. Barbin, and T. Schlick. 2007. Radio Frequency Interference Suppression Techniques in FMCW Modulated HF Radars. Paper presented at the OCEANS 2007 - Europe, 18-21 June.

Gurgel, Klaus W., Heinz H. Essen, and Simon P. Kingsley. 1999. “High-Frequency Radars: Physical Limitations and Recent Developments.” *Coastal Engineering* 37 (3): 201–218. https://doi.org/10.1016/S0378-3839(99)00026-5.

Halverson, Mark, Rich Pawlowicz, and Cédric Chavanne. 2017. “Dependence of 25-MHz HF Radar Working Range on Near-Surface Conductivity, Sea State, and Tides.” *Journal of Atmospheric and Oceanic Technology* 34 (2): 447–462. https://doi.org/10.1175/JTECH-D-16-0139.1.

Hashimoto, Noriaki, Lukijanto, and Masaru Yamashiro. 2010. “Verification of a Modified Bayesian Method for Directional Spectrum Estimation with HF Radar.” *Journal of Japan Society of Civil Engineers Ser B2 (Coastal Engineering)* 66 (1): 1411–1415. https://doi.org/10.2208/kaigan.66.1411.

Hashimoto, Noriaki, and Masayuki Tokuda. 1999. “A Bayesian Approach for Estimation of Directional Wave Spectra with HF Radar.” *Coastal Engineering Journal* 41 (2): 137–149. https://doi.org/10.1142/S0578563499000097.

Hasselmann, Klaus. 1971. “Determination of Ocean Wave Spectra from Doppler Radio Return from the Sea Surface.” *Nature Physical Science* 229 (1): 16–17. https://doi.org/10.1038/physci229016a0.

Hisaki, Yukiharu. 1996. “Nonlinear Inversion of the Integral Equation to Estimate Ocean Wave Spectra from HF Radar.” *Radio Science* 31 (1): 25–39. https://doi.org/10.1029/95RS02439.

Hisaki, Yukiharu. 2015. “Development of HF Radar Inversion Algorithm for Spectrum Estimation (HIAS.” *Journal of Geophysical Research: Oceans* 120 (3): 1725–1740.

IOC, SCOR, and IAPSO. 2010. “The International Thermodynamic Equation of Seawater – 2010: Calculation and Use of Thermodynamic Properties.” *Intergovernmental Oceanographic Commission, UNESCO Manuals and Guides No* 56 (203): 196. https://unesdoc.unesco.org/ark:/48223/pf0000188170.

Kataoka, Tomoya, and Hiroshi Nagamatsu. 2016. “A Bayesian Inversion for Estimating the Directional Spectrum of Ocean Waves in Shallow Water Using HF Radar.” *Journal of Japan Society of Civil Engineers Ser B2 (Coastal Engineering)* 72 (2): I__1711–I__6. https://doi.org/10.2208/kaigan.72.I_1711.

Lipa, Belinda J., and Donald E. Barrick. 1986. “Extraction of Sea State from HF Radar Sea Echo: Mathematical Theory and Modeling.” *Radio Science* 21 (1): 81–100. https://doi.org/10.1029/RS021i001p00081.

Maresca, S., J. Horstmann, R. Grasso, M. Coffin, K. Gurgel, and T. Schlick. 2011. Performance Assessment of HF-Radar Ship Detection. Paper presented at the 2011 12th International Radar Symposium (IRS), Leipzig, Germany, September 7–9. https://ieeexplore.ieee.org/document/6042107.

Noriaki, Hashimoto, Lucy R. Wyatt, and Shoichiro Kojima. 2003. “Verification of a Bayesian Method for Estimating Directional Spectra from HF Radar Surface Backscatter.” *Coastal Engineering Journal* 45 (2): 255–274. https://doi.org/10.1142/S0578563403000725.

Press, William H., Saul A. Teukolsky, William T. Vetterling, and Brian P. Flannery. 2007. “Numerical Recipes.” In *The Art of Scientific Computing*, 1235. 3rd ed. New York, USA: Cambridge University Press.

Ramos, Rafael J., Hans C. Graber, and Brian K. Haus. 2009. “Observation of Wave Energy Evolution in Coastal Areas Using HF Radar.” *Journal of Atmospheric and Oceanic Technology* 26 (9): 1891–1909. https://doi.org/10.1175/2009JTECHO631.1.

Roarty, Hugh, Thomas Cook, Lisa Hazard, Doug George, Jack Harlan, Simone Cosoli, Lucy Wyatt, et al. 2019. “The Global High Frequency Radar Network.” *Frontiers in Marine Science* 6:164. https://doi.org/10.3389/fmars.2019.00164.

Tian, Z., Y. Tian, B. Wen, S. Wang, J. Zhao, W. Huang, and E. W. Gill. 2020. “Wave-Height Mapping from Second-Order Harmonic Peaks of Wide-Beam HF Radar Backscatter Spectra.” *IEEE Transactions on Geoscience & Remote Sensing* 58 (2): 925–937. https://doi.org/10.1109/TGRS.2019.2941823.

Toguchi, Yu, and Satoshi Fujii. 2023. “Quantitative Assessment of Sea Surface Salinity Estimates Using a High-Frequency Radar in Ise Bay, Japan.” *Remote Sensing* 15 (12). https://doi.org/10.3390/rs15123088.

Weber, B. L., and D. E. Barrick. 1977. “On the Nonlinear Theory for Gravity Waves on the Ocean’s Surface. Part I: Derivations.” *Journal of Physical Oceanography* 7 (1): 3–10. https://doi.org/10.1175/1520-0485(1977)007<0003:OTNTFG>2.0.CO;2.

Wyatt, L. R. 2005. “HF Radar for Real-Time Current, Wave and Wind Monitoring.” *Hydro International* 9 (3): 30–31.

Wyatt, L. R., J. J. Green, A. Middleditch, M. D. Moorhead, J. Howarth, M. Holt, and S. Keogh. 2006. “Operational Wave, Current, and Wind Measurements with the Pisces HF Radar.” *IEEE Journal of Oceanic Engineering* 31 (4): 819–834. https://doi.org/10.1109/JOE.2006.888378.

Wyatt, Lucy R., and J. Jim Green. 2009. Measuring High and Low Waves with HF Radar. Paper presented at the OCEANS 2009-EUROPE, 11-14 May.

Wyatt, Lucy R., Guennadi Liakhovetski, Hans C. Graber, and Brian K. Haus. 2005. “Factors Affecting the Accuracy of SHOWEX HF Radar Wave Measurements.” *Journal of Atmospheric and Oceanic Technology* 22 (7): 847–859. https://doi.org/10.1175/JTECH1728.1.

Appendix A: Bayesian inversion method (BIM) to estimate ocean wave spectra

Hashimoto and Tokuda (1999) established a method for inversely estimating the two-dimensional wave spectra in a frequency-direction domain (hereinafter referred to as the “directional spectrum”) from the Doppler spectra based on the Bayesian theorem (BIM). First, the directional spectrum is discretized as follows.

$$S(\omega,\theta) = \exp\left(x_{i,j}\right) \tag{A1}$$

where $i(= 1, 2, \ldots, I)$ and $j(= 1, 2, \ldots, J)$ are the wave frequency and direction numbers, respectively. In addition, I and $J$are the numbers of discretizations in the wave frequency and direction dimensions, respectively. Eq. (A1) satisfies the nonnegative condition of the directional spectrum (i.e., $S(\omega,\theta) > 0$). The directional spectrum can be converted into the wavenumber spectrum $S(\mathbf{k})$ using the following linear dispersion relation:

$$S(\omega,\theta) = \left(\frac{1}{k}\frac{\partial\omega}{\partial k}\right)^{-1} S(\mathbf{k}) \tag{A2}$$

where the linear dispersion relation is expressed by

$$\omega^2 = gk\tanh(kh) \tag{A3}$$

By substituting Eq (A1) and (A2) into Eq (2), the nonlinear algebraic equation $\mathbf{s}(\mathbf{x})$ for the second-order cross-section with the unknown vectors $\mathbf{x} = \left(x_{1,1}\cdots x_{i,j}\cdots x_{I,J}\right)^t$, which express the directional spectrum, can be obtained. Note that the superscript t indicates transposition. Consequently, the Doppler spectra can be expressed as follows.

$$\mathbf{d} = \mathbf{s}(\mathbf{x}) + \mathbf{e} \tag{A4}$$

$$\begin{cases} d = (d_1\cdots d_k\cdots d_K)^t \\ s(\mathbf{x}) = (s_1(\mathbf{x})\cdots s_k(\mathbf{x})\cdots s_K(\mathbf{x}))^t \\ e = (e_1\cdots e_k\cdots e_K)^t \end{cases}$$

where $\mathbf{d}$ is the vector of the dimensionless Doppler spectrum in which the second-order power is divided by the sum of first-order peak powers in negative and positive domains. Likewise, $\mathbf{s}(\mathbf{x})$ is the vector of the dimensionless scattering cross-section in which the second-order cross-section is divided by the first-order cross-section. This normalization is derived from the proportional relationship between the scattering intensity and the cross-section (Hisaki 1996). In addition, $\mathbf{e}$ is the error vector of the observed Doppler spectra, which is normally distributed. The subscripts$k(= 1, 2, \cdots, K)$ are the indexes of the Doppler frequency.

In the BIM, the following posterior probability distribution considering the smoothness of the directional spectrum is maximized to determine an optimal solution:

$$p\left(\mathbf{x},\alpha^2,\gamma^2|\mathbf{d}\right) = z^{-1}\left(\alpha^2\right)^{-\frac{K+L}{2}}\left(\gamma^2\right)^{\frac{L}{2}}\exp\left[-\left(2\alpha^2\right)^{-1}f(\mathbf{x})\right], \tag{A5}$$

$$f(\mathbf{x}) = |\mathbf{d} - \mathbf{s}(\mathbf{x})|^2 + \gamma^2|\mathbf{D}\mathbf{x}|^2. \tag{A6}$$

where z^{-1} is a normalization constant and L is the matrix size of the discretized directional spectrum ($= I \times J$). α^2 and γ^2 are hyperparameters that determine the likelihood function and posterior probability distribution, respectively. $\mathbf{Dx}$ is derived from the prior information for determining the smoothness of the directional spectrum (Hashimoto and Tokuda 1999; Hashimoto, Lukijanto, and Yamashiro 2010; Noriaki, Wyatt, and Kojima 2003). γ^2 determines the dependence of an estimated directional spectrum on the observation errors (the first term of Eq (A6)) and the prior information (the second term of Eq (A6)). The directional spectrum is dependent on the Doppler spectrum if γ^2 is small; however, this depends on the prior information if γ^2 is large. After all, the directional spectrum can be estimated by maximizing Eq (A5), in other words, by minimizing Eq (A6).

To determine the optimal solution of $\mathbf{x}$, Akaike’s Bayesian Information Criterion (ABIC; Akaike (1980)) can be determined through Eq. (A7).

$$ABIC = -2\ln\int p\left(\mathbf{x},\alpha^2,\gamma^2|\mathbf{d}\right)d\mathbf{x}. \tag{A7}$$

In the present study, the optimal hyperparameters γ_o^2 were searched by applying the golden-section search (Press et al. 2007). The initial interval of γ^2 was selected as $\left[\gamma_l^2, \gamma_u^2\right] = \left[10^{-3}, 1\right]$, and then the ABIC was iteratively computed until it satisfied $\left|ABIC\left(\gamma_2^2\right) - ABIC\left(\gamma_1^2\right)\right| < 10$. Finally, the optimal solution of $\mathbf{x}$ is obtained, which is $\mathbf{x}_o$. By using $\mathbf{x}_o$, the significant wave height is calculated as

$$H_s = 4.0\sqrt{E_0} \tag{A8}$$

where E_0 is the total wave energy by integrating the directional spectrum with respect to wave frequency and direction as follows.

$$E_0 = \int_0^\infty\int_{-\pi}^{\pi} S(\omega,\theta)d\theta d\omega. \tag{A9}$$